

# Low-density expanded perlite–aluminium syntactic foam

M. Taherishargh\*, I.V. Belova, G.E. Murch, T. Fiedler

Centre for Mass and Thermal Transport in Engineering Materials, Discipline of Mechanical Engineering, University of Newcastle, University Drive, Callaghan, NSW 2308, Australia

## ARTICLE INFO

### Article history:

Received 10 February 2014

Received in revised form

28 February 2014

Accepted 1 March 2014

Available online 12 March 2014

### Keywords:

Syntactic foam

Expanded perlite

Infiltration

Mechanical characterization

Electron microscopy

## ABSTRACT

This paper addresses an innovative syntactic foam (SF) formed by counter-gravity infiltration of a packed bed of low-cost expanded perlite (EP) particles with molten A356 aluminium. The uniform distribution of EP particles in foams causes an even density throughout the height. Due to the low density ( $\sim 0.18 \text{ g/cm}^3$ ) of EP, the average density of these foams is only  $1.05 \text{ g/cm}^3$  which is considerably lower than most studied SFs. Owing to the high porosity of the filler material ( $\sim 94\%$ ), the total porosity of the new foam reaches 61%. Microstructural observations reveal no sign of damage or unintended EP particle infiltration. EP shows a good wettability whilst essentially no reaction occurs at the EP–metal interface. Under compression, EP/A356 syntactic foam shows stress–strain curves consisting of elastic, plateau and densification regions. On account of its consistent plateau stress (average value  $30.8 \text{ MPa}$ ), large densification strain (almost 60%), and high energy absorption efficiency (88%) EP/A356 syntactic foam is an effective energy absorber.

© 2014 Elsevier B.V. All rights reserved.

## 1. Introduction

In recent years, metal matrix syntactic foams (MMSFs) have been studied extensively because of their superior mechanical and energy absorbing properties and relatively lower cost in comparison with conventional metal foams [1–4]. By definition, MMSFs consist of a metallic matrix containing hollow or porous particles [1,2,5]. Such foams can be produced by powder metallurgy [6] or stir casting [5]. Pressure infiltration is probably the most promising process due to its lower cost and a higher achievable volume fraction of filler particles [7].

The minimum achievable density of MMSFs is higher than that of metallic foams [6,8,9]. This has been a major limitation. The density of MMSFs is determined by the volume percentage and density of filler material. The volume percentage of randomly packed, similar size filler particles barely exceeds about 64%, the dense random packing density of mono-size spheres [2,7,10,11]. Thus one can say the density of MMSFs depends largely upon the density of the filler particles [10]. Over the last two decades, various types of hollow particles (hollow spheres (HS)) including metal [12–14], ceramic [8], carbon [15], glass [5,16], and fly ash (cenospheres) [17,18] have been used in the preparation of MMSFs. However, such particles have a relatively high density, reportedly more than  $0.6 \text{ g/cm}^3$  (see Table 1) [6,19,20] which limits the minimum density of MMSFs. In addition,

unintended infiltration of the spheres caused by failure of the filler particle shell can increase the density of MMSFs [21,22]. Because of the above reasons, the minimum reported aluminium syntactic foam densities are typically greater than about  $1.4 \text{ g/cm}^3$  (see Table 1) [7,19,22,23].

Generally, HSs are produced synthetically via methods such as sol–gel processes, sacrificial core, or nozzle blowing [24] which add to the cost of the MMSF. As a by-product of coal-fired power plants [5,18], cenospheres are the most cost effective filler materials. However, their size limitation (typically less than  $300 \mu\text{m}$ ) dictates the need for a complicated infiltration process [1].

Up till now, the application of ceramic and glass HSs in MMSFs has been broadly investigated, but there are limited reports on utilizing porous particles [4]. In this context, HSs refer to filler particles with a solid or porous skin containing one large internal cavity whereas a porous particle describes geometries that contain a multitude of small pores. In this paper, we propose the use of porous expanded perlite (EP) particles to produce low-cost low-density aluminium syntactic foam.

EP is produced by heating raw perlite rock to  $870^\circ\text{C}$ . Raw perlite is a hydrated silicate base volcanic glass typically containing 2–6 vol% of water in its structure [25,26]. Perlite is expanded to 15–20 times of its original volume due to the large volume change of trapped water during its liquid–vapor phase transition in the softened structure. [27]. The content of  $\text{SiO}_2$  is more than 70%, which is 10% more than that of a typical glass or ceramic HS [28], while the  $\text{Na}_2\text{O}/\text{K}_2\text{O}$  ratio is less than one [27]. Owing to its low density, high porosity, chemical inertness, fire resistance and

\* Corresponding author. Tel.: +61 432620029.

E-mail address: [Mehdi.Taherishargh@uon.edu.au](mailto:Mehdi.Taherishargh@uon.edu.au) (M. Taherishargh).

**Table 1**  
Data of some studied MMSFs.

Matrix	Filler material	Filler size	Filler particle density (g/cm <sup>3</sup> )	MMSF density (g/cm <sup>3</sup> )	Total volume porosity %	Ref.
Pure Al	Cenosphere	90–150 $\mu\text{m}$	1.00–0.74	1.52–1.43	40.7–43.7	[1]
A356	Cenosphere	45–250 $\mu\text{m}$	0.7	1.25–2.1		[17]
Al4047	Ceramic HS: 33Al <sub>2</sub> O <sub>3</sub> –48SiO <sub>2</sub> –19 Mullite	150 $\mu\text{m}$	0.6	1.35		[16]
Pure Al	Ceramic HS: 45 SiO <sub>2</sub> –35 Al <sub>2</sub> O <sub>3</sub> –20 Mullite	100–1450 $\mu\text{m}$	0.57–0.81	1.43–1.49	41–47.6	[11]
Pure Al	Ceramic HS: 60SiO <sub>2</sub> –40Al <sub>2</sub> O <sub>3</sub>	250–500 $\mu\text{m}$	0.75	1.38	51	[4]
Al 6082	Ceramic HS: 60SiO <sub>2</sub> –40Al <sub>2</sub> O <sub>3</sub>	75–125	0.6	1.45		[2]
A356	Ceramic HS: SiC	1 mm	1.160	1.819	38	[8]
Al2024	Ceramic HS: Alumina	3–4.25 mm	1.25	1.25		[9]
Pure Al	Glass HS: 60SiO <sub>2</sub> –15Al <sub>2</sub> O <sub>3</sub> –15CaO–10Na <sub>2</sub> O	0.5–4 mm	0.95–0.65	1.58–1.88	44–31	[4]

sound absorption, EP has been broadly used in asphalt, resin-based castings, combating oil spillage [25], filtration systems [29], and construction elements [26,27]. In the present study, EP/A356 Al alloy syntactic foam was fabricated by a counter gravity infiltration technique. The structure and density of the foam and EP particles were investigated. The interface between the EP particles and base metal was examined and mechanical properties of the foam were evaluated.

## 2. Materials and experimental procedures

### 2.1. Materials

EP particles were obtained from Australian Perlite Pty and particles with a size range of 3–4 mm were used. According to their product data sheet, EP particles have the composition of 75 wt% SiO<sub>2</sub>, 14 wt% Al<sub>2</sub>O<sub>3</sub>, 3 wt% Na<sub>2</sub>O, 4 wt% K<sub>2</sub>O, 1.3 wt% CaO, 1 wt% Fe<sub>2</sub>O<sub>3</sub>, 0.3 wt% MgO, 0.2 wt% TiO<sub>2</sub> with traces of heavy metals. A356 aluminium alloy with the composition of 7.2 wt% Si, 0.4 wt% Mg, 0.1 wt% Fe, and 0.12 wt% Ti was used as the matrix metal. Because of its high Si content, it has good castability, a short solidification time, good resistance to hot cracking and a low solidification shrinkage [17,21]. The presence of Si and Mg results in improved mechanical properties in both plain and heat-treated conditions [30]. Moreover, the Mg content of the alloy improves the wettability of the particles [31].

### 2.2. Experimental procedures

The counter-gravity pressure infiltration equipment used for the manufacturing of the syntactic foam is illustrated in Fig. 1. Prior to casting, EP particles were dried in a furnace for 30 min at 250 °C. In order to minimize the oxidation of the aluminium, filling and assembling of the components shown in Fig. 1 took place inside a glove-box containing a controlled argon atmosphere. In the glove-box antechamber, EP particles and set-up parts were exposed to a low vacuum ( $10^{-4}$  MPa) followed by purging with argon gas (0.1 MPa). This procedure was repeated three times. Inside the glove-box, a stainless steel mesh was placed at the graphite mould ventilation hole to prevent particles from blocking it. To achieve uniform tightly packed EP particles, the graphite mould was filled in five equally sized batches and vibrated for 1 min after each step. The EP particles mass ( $m_p$ ) was measured by subtracting the weight of the mould before and after filling (correcting for the mass of the stainless mesh). A second stainless steel mesh packed the mould to both guard against the displacement of EP particles and filter any possible aluminium oxide on the surface of the molten metal. A block of room temperature A356 alloy was placed in a graphite crucible and the filled mould was rotated and placed on top of it. The volume of the solid aluminium was twice the combined volume of the EP particles to

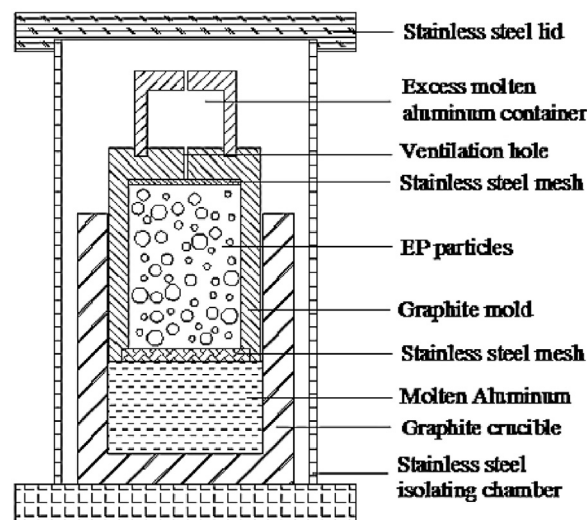


**Fig. 1.** Counter-gravity pressure infiltration set-up for producing EP/A396 Al syntactic foam.

ensure full infiltration during casting. The assembled crucible was put into a stainless steel isolating chamber (SSIC) that maintained the protective argon atmosphere. After removal from the glove-box, the assembly was placed in an electric furnace and heated from room temperature to 720 °C and held at this temperature for 30 min. Then, the assembly was removed from the furnace and the stainless steel lid of the SSIC was removed. The mould was pushed downwards within the graphite crucible thus forcing the molten aluminium into the graphite mould causing infiltration. Two 1 mm diameter ventilation holes allowed the escape of air and excess aluminium. The assembly was cooled down under atmospheric conditions. Finally, the sample was manually pushed out of the mould. The upper and lower surfaces of the cylindrical sample were machined to remove the stainless steel meshes.

Samples for metallography were cut from the as-infiltrated EP/A356 syntactic foam using a low-speed silicon carbide saw. They were polished using SiC paper, followed by 6  $\mu\text{m}$  and 1  $\mu\text{m}$  water-based diamond suspensions. The microstructure of EP particles and syntactic foam was examined using scanning electron microscopy (FEI XL30 SEM) and optical microscopy. The elemental X-ray mapping of the EP-A356 alloy interface was investigated by a JEOL 6100 SEM equipped with an Oxford ISIS EDS system.

To evaluate the uniformity and distribution of the EP particles, micro-computed tomography ( $\mu\text{CT}$ ) imaging with a spatial resolution of 48.2  $\mu\text{m}$  was performed. In addition, to investigate the density gradient, samples were accurately cut in equal pieces with 7 mm height and the volume and mass (density) of each piece was measured. The height ( $h$ ) and diameter ( $d$ ) of the samples were measured with a precision electronic calliper to calculate the volume of the cylindrical sample (i.e.  $V_{\text{sf}} = 1/4\pi d^2 h$ ). The density

was determined by way of dividing the weight of the sample by this volume.

Mechanical properties of EP/A356 syntactic foam were examined by performing compression tests according to the ISO 13314 standard on cylindrical samples with the diameter of 30 mm and the height of 45 mm. A uni-axial computer-controlled 50 kN Shimadzu testing machine was used at a crosshead speed of 1 mm/min. The compressive loading plates were well lubricated to minimize friction effects. During the test, the load and cross-head displacement data was recorded via built-in data acquisition software (Trapezium2) and subsequently converted to engineering stress–strain curves based on the initial sample cross sectional area and height.

### 3. Results and discussion

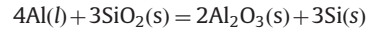
#### 3.1. Microstructural characterization

Fig. 2 shows SEM images of the porous outer surface (a) and mid-cross-section (b) of an EP particle. It can be seen that the outer surface of the EP particle is covered with open pores, i.e. the surface does not appear solid. Fig. 2b indicates that the pores are approximately uniform in size and exhibit a frothy-like structure. The angle of  $120^\circ$  between the cell walls implies that the EP internal structure is mainly composed of closed cells with a dodecahedron geometrical shape. This geometry explains the crushing resistance of the EP particles despite their thin and brittle cell walls [32].

Fig. 3a shows the SEM image of an EP particle embedded in the A356 matrix. The full envelopment of the EP particle by the matrix shows that the particles have a good wettability under the given process conditions. Also, despite the poor mechanical properties of brittle EP particles, they remain intact during infiltration. No damage or failure was observed even in areas near the particle

surface. Furthermore, the molten metal does not penetrate into the EP particles thereby resulting in a smooth interface. This can be seen in Fig. 3b that shows the metal matrix where an EP particle has been removed. Apparently, the pressure of the infiltration process is insufficient to overcome the high surface tension of molten metal for the impregnation of the open pores within the EP. In the case of hollow spheres, infiltration of the particle because of shell failure is known to increase the MMSF density [21,22]. Due to their porous structure, even damaged EP particles cannot be fully infiltrated with liquid metal.

Next, a possible chemical reaction between metal and EP particles is addressed. Like most filler materials, EP is predominantly composed of  $\text{SiO}_2$  which can react with Al [7,16,21,33] according to:



$$\Delta G = -310 \text{ to } -330 \text{ kJ mol}^{-1}, 700\text{--}850^\circ\text{C} \quad (1)$$

In this reaction, amorphous  $\text{SiO}_2$  transforms to crystalline  $\alpha\text{-Al}_2\text{O}_3$  and Si inclusions precipitate along the interface [34,35]. The formation of  $\text{Al}_2\text{O}_3$  at the interface may increase the local stiffness but a change of silicon content degrades the aging properties [21]. In addition, the density of foam increases by degradation and failure of the wall of the fillers as a result of this reaction [7].

The well-known A356 Al alloy solidification structure consists of a eutectic constituent of aluminium-rich phases and silicon phases grown between the primary dendritic networks (Fig. 4a). X-ray mapping of oxygen at the interface area shown in Fig. 4b is recorded with  $\text{OK}_\alpha$  and shown in Fig. 4c where concentrations of oxygen are indicated by bright spots. Fig. 4c shows no oxygen concentrations (bright spots) at the particle–matrix interface. The oxygen is evenly distributed in the scanning area meaning that no significant amount of  $\text{Al}_2\text{O}_3$  was formed at the interface. This is a clear indication that the chemical reaction (1) is not significant for this system under our

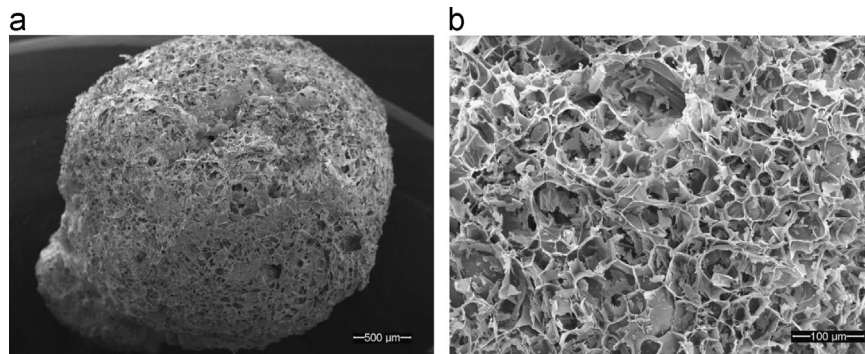


Fig. 2. SEM image of (a) EP particle surface; (b) EP particle cross section.

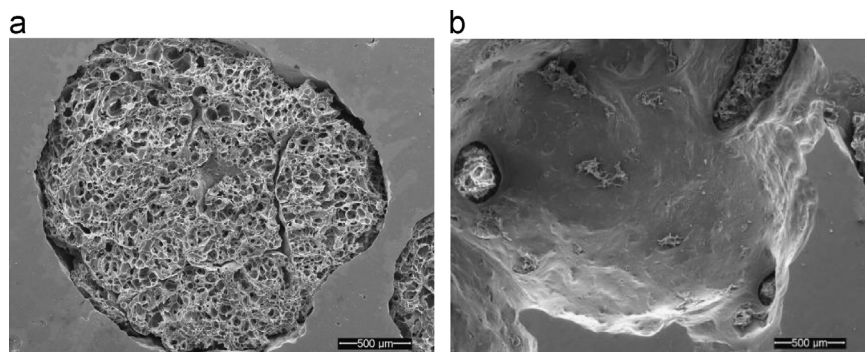


Fig. 3. SEM image of the (a) EP in A356 Al matrix, and (b) empty space of removed EP particle.



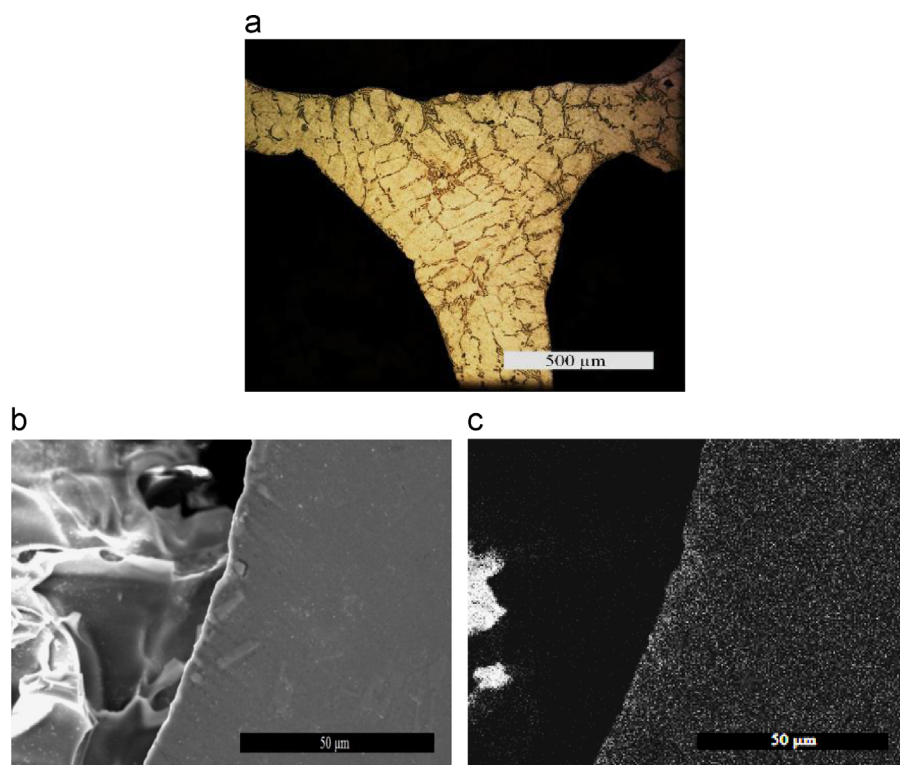


Fig. 4. (a) Optical microscope micrograph of base metal, (b) SEM image of the EP/A356 Al interface, (c) X-ray map for the distribution of oxygen.

conditions. One can assume that the uniform aluminium surface oxide layer is the source of the detected oxygen.

The kinetics of the reaction (Eq. (1)) is controlled by chemical reaction and atomic diffusion [35]. Accordingly, the infiltration temperature and time [7,36–38], and silicon content of molten metal [7,39] are the major parameters that determine the extent to which this reaction occurs. Studies have shown that in the case of pure Al and SiO<sub>2</sub> below 900 °C the products of Eq. (1) are not detectable, meaning that the growth rate of the reacted layer is very low [40]. Furthermore, the thickness of the reacted layer decreases linearly with decreasing time [38–40]. Thus, the chemical reaction at the interface of EP and molten metal is negligible because of the low temperature of the process (720 °C) and the short solidification time (less than one minute based on observations). It can also be noted that the high Si content (7 wt%) of the A356 alloy reduces the difference in chemical potential between the interface and the adjacent region. This will limit the diffusion fluxes of both Si and Al and further reduce reaction rate [16].

### 3.2. Density evaluations

A sample of EP/Al356 syntactic foam is shown in Fig. 5a. Fig. 5b shows orthogonal slices of a μCT scan of the syntactic foam. It can be observed that the EP particles are distributed in a relatively uniform way throughout the height and diameter of the sample. A classification system for a mathematical description of composite structure morphology as developed by Michelsen et al. [41] based on Minkowski functionals was applied to the μCT images. The metal matrix phase of the considered material has the following functionals: relative density  $V=0.37$ , normalized surface area  $S=5.15$ , normalized mean breadth  $B=-7.28$  and normalized Euler characteristic  $\chi=5.82$ .

In the fabrication process, the mould is filled with EP particles prior to infiltration. The mould can be either filled in one step or multiple steps (layer by layer) combined with vibration. The uniformity in structure of the foams is a result of the five-step

filling which reduces the density gradient accompanied with one step filling [33]. To have a more accurate understanding of the filling process effect on the particles and density distribution, samples # 6 and 7, produced by five and one step filling respectively, were sectioned. Fig. 6 shows the density plotted versus the sample height. It can be seen that the filling procedure strongly affects the density gradient. In the case of one-step filling, inter-particle friction limits the ability of the particles to form dense packing arrangements as the mould is vibrated. Particles in lower parts have a decreased mobility and a cluster of particles can form an arc or bridge-like arrangement leaving large voids beneath. This can result in a considerable density gradient as shown in the figure. However, the five-step filling process, accompanied with vibration after each step, minimizes the effect of interparticle friction and creates denser packing arrangements. This results into a lower overall foam density with more homogeneity. Accordingly, all of the foams used in this study were produced by a five-step filling procedure.

The average density of samples 1–6 was 1.05 g/cm<sup>3</sup> (see Table 2). This is considerably below the typical densities for syntactic aluminium foams (see Table 1). This low density can be explained by the absence of unintended EP particle infiltration with aluminium (see Fig. 3a and c) and the low density of EP particles in comparison to currently used filler materials.

The volume fraction of EP particles ( $F_p$ ) can be calculated as

$$F_p = \left( \frac{V_{sf} - ((m_{sf} - m_p)/\rho_{Al})}{V_{sf}} \right) \times 100 \quad (2)$$

where  $V_{sf}$  is the foam volume,  $m_p$  is the combined perlite mass,  $m_{sf}$  is the syntactic foam mass, and  $\rho_{Al}$  is the density of aluminium (2.68 g/cm<sup>3</sup> according to the mixing rule). The average volume fraction of EP particles in samples 1–6 was 65% (see Table 2) which slightly exceeds the maximum volume fraction of randomly packed mono-sized spherical particles [2,7,10,11]. A likely explanation for the high packing density is that the perlite particles are

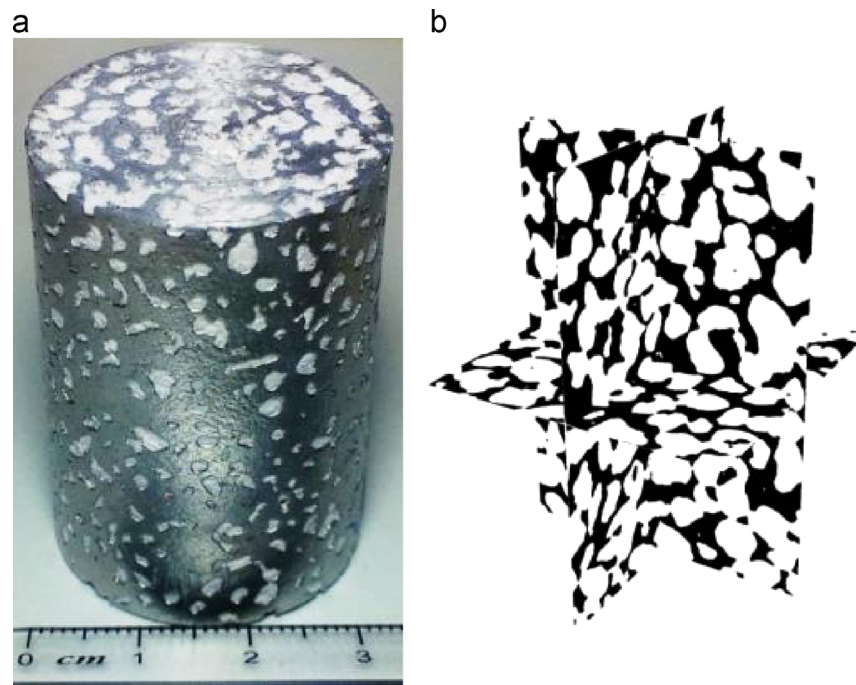


Fig. 5. (a) Produced EP/A356 Al syntactic foam, (b) orthogonal slices of  $\mu$ CT data.

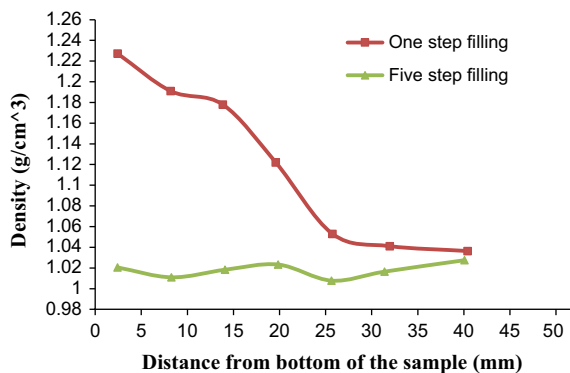


Fig. 6. The density over the height of the samples produced with one and five step filling.

Table 2  
Samples information.

No.	EP mass (g)	Foam mass (g)	Foam volume (cm <sup>3</sup> )	Foam density (g/cm <sup>3</sup> )	EP volume fraction (%)	Total porosity (%)
1	3.85	33.51	32.01	1.05	65.43	61.2
2	3.39	32.92	31.2	1.06	64.70	60.9
3	3.71	35.13	32.27	1.09	63.72	59.6
4	3.06	33.91	31.64	1.09	63.07	59.6
5	3.38	34.65	31.75	1.09	63.30	59.5
6	3.52	32.74	32.2	1.02	66.14	62.2
7	3.55	36.00	31.8	1.13	61.96	57.9

not perfectly spherical and are not monosized (their size varies in the range of 3–4 mm).

Assuming that no unintended EP particles infiltration occurred, the density of EP particles ( $\rho_p$ ) can be calculated as

$$\rho_p = \frac{m_p}{V_{sf} - ((m_{sf} - m_p)/\rho_{Al})} \quad (3)$$

Based on Eq. (2) and the data in Table 2, the average EP particle density was found to be 0.18 g/cm<sup>3</sup>. It should be noted that this

value is less than one third of the minimum reported density of common filler materials (see Table 1). Based on the perlite mass fractions and constituents the densities of SiO<sub>2</sub>, Al<sub>2</sub>O<sub>3</sub>, CaO, Na<sub>2</sub>O, K<sub>2</sub>O, Fe<sub>2</sub>O<sub>3</sub>, MgO, and TiO<sub>2</sub> are 2.65, 3.97, 3.34, 2.27, 2.35, 5.24, 3.58 and 4.23 g/cm<sup>3</sup>, respectively [4], the density of the solid part of the perlite particles ( $\rho_s$ ) is estimated to be 2.79 g/cm<sup>3</sup>. This means that about 94% of the EP particle volume is porosity which is in agreement with the reported porosities in [25,26]. Since the porosity of the syntactic foam is determined by the porosity of the filler material [10], the high porosity of EP results in a high total porosity of syntactic foam ( $F_{TP}$ ) which can be calculated according to:

$$F_{TP} = F_p \times \left(1 - \frac{\rho_p}{\rho_s}\right) \quad (4)$$

The average  $F_{TP}$  of the syntactic foam samples is 61%. Comparing this value to the data in Table 1 it becomes clear that this is certainly a high value for a MMSF.

### 3.3. Compressive response

The compression tests were carried out on samples #1–5 (see Table 2) (samples #6 and 7 were destroyed to obtain the density profile shown in Fig. 6). The quasi-static compressive engineering stress–strain curves are shown in Fig. 7. The EP/A356 syntactic demonstrates a compressive behaviour that is typical for metallic foams. The stress–strain curves exhibit three distinct stages which are marked approximately in Fig. 7: (I) linear elastic deformation, (II) stress plateau in which the compaction and plastic deformation occurs at an approximately constant stress level and (III) densification where the foam porosity is significantly decreased after large plastic deformation.

Fig. 8 schematically shows the method of obtaining mechanical characteristics via the stress–strain curve according to ISO 13314 standard. The first maximum compressive stress (FMCS) corresponds to the first local maximum in the stress–strain curve. The plateau stress ( $\sigma_{pl}$ ) is an important design factor for cushions or impact mitigation. The stress  $\sigma_{pl}$  was obtained as the arithmetic mean of stresses between 20% and 40% of macroscopic

compressive strain. The plateau end stress ( $\sigma_{ple}$ ) is defined as 1.3 times the plateau stress. The energy absorption per unit volume ( $W$ ) was calculated as the integral of the stress–strain curve up to 50% strain according to:

$$W = \int_0^{\epsilon_{50\%}} \sigma d\epsilon \quad (5)$$

The energy absorption efficiency ( $\eta$ ) is a second parameter that describes the ability of the material for energy absorption. It is defined as the ratio of absorbed energy to the energy absorption of an ideal absorber. An ideal absorber directly reaches the maximum possible stress after yielding which remains constant during deformation [42]. Thus,  $\eta$  is defined as

$$\eta = \frac{\int_0^{\epsilon_{50\%}} \sigma d\epsilon}{\sigma_{max} \epsilon_{50\%}} \times 100 \quad (6)$$

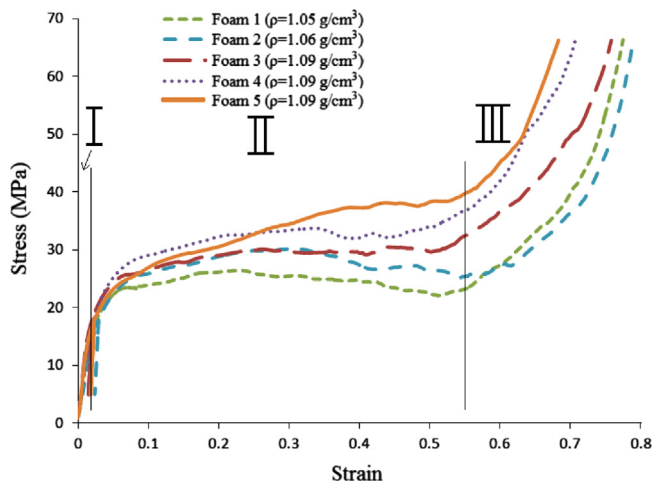


Fig. 7. Compressive engineering stress–strain curves of EP/A356 syntactic foams.

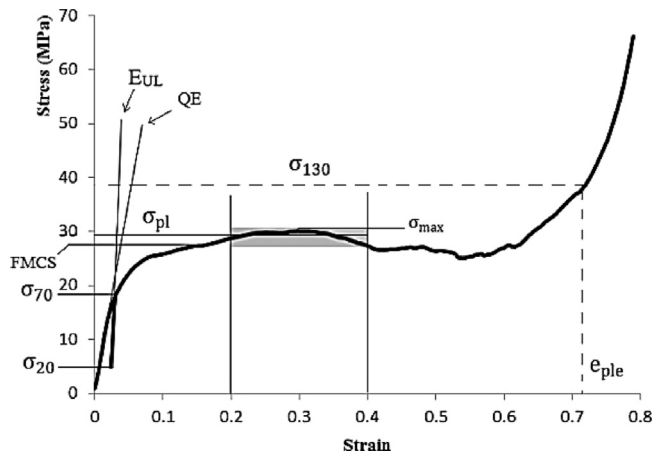


Fig. 8. Engineering stress–strain curve of sample #2 and derived material properties.

where  $\sigma_{max}$  is the maximum stress taken by the foam up to 50% strain.

Typically, the gradient of the straight line within the linear deformation region is lower than the real Young's modulus ( $E$ ). Accordingly, it is called the quasi-elastic gradient (QE) which is shown in Fig. 8. An alternative approach to determine the elastic modulus of a cellular metal is to first compress the foam into its plastic range. The structure is then unloaded and the elastic modulus  $E_{UL}$  is obtained from the unloading slope (see Fig. 8). To this end, an initial sample was tested to gain the corresponding plateau stress. The next four samples were loaded to 70% of the plateau stress  $\sigma_{70}$  and unloaded to 20% of the plateau stress  $\sigma_{20}$ .

The calculated mechanical properties of the EP/A356 syntactic foam are shown in Table 3. The results show that although the densities of the samples are similar, a slight increase in density from 1.05 to 1.09 g/cm<sup>3</sup> enhances  $\sigma_{pl}$ , FMCS, and  $W$ . This is in agreement with the well-accepted principle that the compressive properties of foam increase with its density [43–46]. However, it can be seen that there are additional small differences in mechanical properties of foams with the same density. A likely explanation is the existence of inhomogeneities in the material meso-structure due to variations of the irregular EP particle shape and size as well as random packing. The parameters have low variance since the coefficients of variation for  $\sigma_{pl}$ , plateau end strain  $e_{ple}$ ,  $W$ , and  $\eta$  are 7.5%, 2.5%, 6.1%, and 5.56% respectively.

As shown in Fig. 8 and Table 3, the unloading modulus  $E_{UL}$  is significantly higher than the quasi-elastic parameter QE. A likely explanation for this deviation is localized plasticity in the specimen where some cells yield at very low loads [47]. As a result, both elastic and plastic deformations contribute in the quasi-elastic gradient. In addition, neither of the surfaces in touch with loading plates are perfectly smooth. At low strains, the load flattens both surfaces until complete contact is established (settling). In contrast, the unloading gradient is purely elastic and not affected by settling of the sample. However, it should be noted that  $E_{UL}$  is merely an approximation of Young's modulus of the material [48]. It depends on the porosity of the foam at the unloading strain and decreases with compressive deformation up to a specific strain after which it increases [49,50].

Considering the plateau stress and energy absorption, the effect of a slight density alteration is significant. Foam 5 absorbs considerably more energy than Foam 1 despite having a lower densification strain. It is associated with a significantly higher plateau stress of Foam 5. All foams show a high energy absorption efficiency (calculated for 50% strain). The reported  $\eta$  for some metallic syntactic foams varies in the range of 65–80% [42,51–53]. Although, the absorbed energy increases with density, there is no correlation between the energy absorption efficiency and the density. A higher  $\eta$  is primarily attributed to a smoother plateau region without sharp stress oscillations.

It is of interest to compare the mechanical properties of the EP/A356 syntactic foam with open cell foams made of the same matrix material and with a similar pore size. An A356 open cell foam was produced by infiltration of spherical soluble sulphate particles with a diameter of 3 mm [54]. This foam showed similar

**Table 3**  
Mechanical properties of EP/A356 syntactic foams.

	$\rho$ (g/cm <sup>3</sup> )	QE (GPa)	$E_{UL}$ (GPa)	$\sigma_{pl}$ (MPa)	FMCS (MPa)	$\sigma_{ple}$ (MPa)	$e_{ple}$ (%)	$W$ (MJ/m <sup>3</sup> )	$\eta$ (%)
#1	1.05	1.02	–	25.42	23.07	33.05	65	11.89	90
#2	1.06	0.79	2.32	29.36	27.36	38.17	71	13.25	88.1
#3	1.09	1.35	2.59	29.6	30.04	38.48	62	13.87	91.1
#4	1.09	1.14	2.74	32.89	32.49	42.76	60	15.14	89.4
#5	1.09	1.36	2.66	34.38	37.2	44.68	59	15.64	81.82



compressive stress–strain curves with a plateau stress  $\sigma_{pl} = 29$  MPa. It should be noted that the sulphate particles were leached out after infiltration (replication process) and thus did not contribute to the mechanical strength of the foam [54]. Based on the similar compressive behaviour, it can be assumed that the analogous perlite particles do not have a significant contribution to the mechanical strength of the EP/A356 syntactic foam. According to microstructural observations the cell wall thickness of EP particles is less than 500 nm. In combination with the brittle material behaviour of solid perlite, EP particles are unable to support a substantial amount of compressive load and strengthen the syntactic foam.

However, the approximately spherical shape of the EP particles benefits the mechanical properties of the cellular aluminium matrix (i.e. the inverse volume of the packed EP particles). In [45] a metallic foam was produced by A356 alloy infiltration of a bed of NaCl particles with the same size range as the EP particles of this study. This foam had a distinctly lower plateau stress  $\sigma_{pl} = 18$  MPa. The authors assumed that the angular shape of NaCl particles is more likely to result in cells with irregular shape and sharp angles. The resulting stress concentrations and heterogeneous distribution of the pores in the matrix due to the angular pore shape deteriorate the mechanical properties [55]. Thus, one can assume that despite not directly improving the mechanical properties, expanded perlite is a good space holder for the production of low-density metallic syntactic foam having high strength. In addition, due to its low density and chemical inertness, there is no requirement for the removal of perlite from the structure.

The mechanical properties of metallic foam strongly depend on the deformation mechanism. The EP/A356 syntactic foam exhibited two different mechanisms during compression tests which are illustrated in Fig. 9. The higher density samples (3, 4 and 5)

showed a uniform deformation with multiple active collapse bands (Fig. 9(a)). In contrast, the samples with lower densities (1 and 2) deformed locally along shear bands (Fig. 9(b)). Such changes of the deformation mechanism due to density variations have already been observed elsewhere [4,56,57].

Sample # 5 (higher density) exhibits a uniform deformation illustrated in Fig. 9(a). In the linear deformation area, no cell distortion was observed at the surface. During further deformation inside the plateau region, the strain appeared to be evenly distributed throughout the sample. In this stage, localized deformation bands initiate at single cells and grow across the entire cross section by cell distortions in the form of bending or buckling. The distorted cells are unlikely to collapse because of strain hardening. Instead, they induce stress concentrations in neighbouring cells which are still within the elastic region and new deformation bands nucleate and grow progressively in different areas [58]. The buckled cell walls in Fig. 9(a) at a macroscopic strain of 34% show the deformation bands formed by successive load transfer. The foam was uniformly deformed and no shear or material protrusions were observed at the surface of the sample during compression at the strains up to 50%. As the densification stage approached, all of the deformation bands collapsed in a layer-by-layer manner which resulted in uniform failure of the material. The strain concentration caused by the collapse of a band initiated the collapse of the neighbouring bands [58].

The samples with the lower density showed a different deformation behaviour. In sample #1 (Fig. 9(b)) localized deformation resulted in the formation of a large shear band with an angle of  $30^\circ$  (with respect to the loading plate) and two smaller bands which are marked in white lines. Typically, deformation bands form at the angles ranging from  $25^\circ$  to  $45^\circ$  [19,58,59]. Beneath the large shear band a dead zone with no significant deformation was observed (indicated by a white triangle). As the deformation

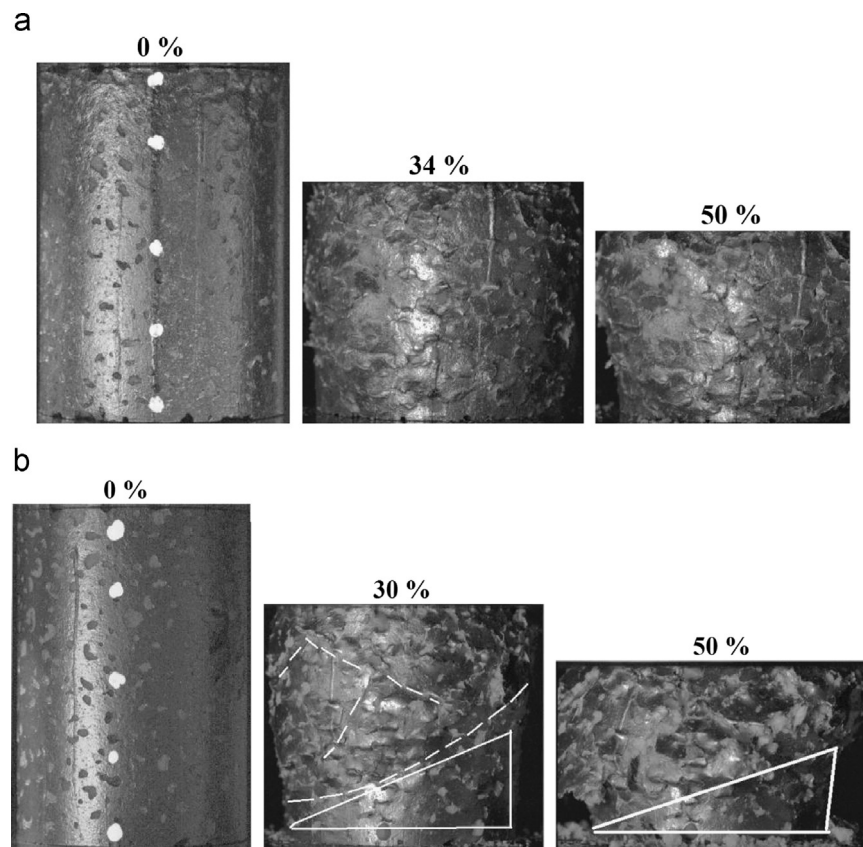


Fig. 9. Representative compressive deformation process of foam samples with densities of (a) 1.09 and (b) 1.05 g/cm<sup>3</sup> at different strains.

proceeded, the material deformation and cell collapse was concentrated inside and above the shear band while the dead zone did not experience significant deformation. The observed multiple active shear bands and protrusions at the edges of the bands on the surface could be indicative of a prevalence of cells tearing and fracture. This means that the strain hardening of cells within the deformation bands failed to cause an effective stress transfer to neighbouring areas before these cells collapse. This may be a reason for the formation of the dead zone.

These different deformation behaviours can be linked to the stress–strain curves shown in Fig. 8. The compressive stress of the low density samples gradually decreases after reaching a critical strain (i.e.  $\epsilon=0.24$  for sample 1 and  $\epsilon=0.32$  for sample 2) because of macroscopic shear. In contrast, the curves of the higher density samples show a steady stress increase most likely due to strain hardening and densification. A decrease in stress prior to densification is not observed in any of the foam samples with higher density.

#### 4. Conclusions

In the present study, we have introduced expanded perlite as a filler material to produce low density ( $1.05 \text{ g/cm}^3$ ) metal matrix syntactic foams via counter-gravity pressure infiltration. Expanded perlite, a commercial material available at low-cost, is a porous glass with approximately 94% porosity. Its low density ( $0.18 \text{ g/cm}^3$ ) is about one third that of common filler materials used in syntactic foams. It showed good wettability under the given process conditions. No unintended infiltration of expanded perlite particles was observed. There was no evidence of chemical reaction between the expanded perlite and the A365 matrix. The syntactic foam samples exhibited a total porosity of 61% which is much higher than that of previous syntactic foams. Uni-axial compressive tests of the material were performed under quasi-static conditions. The EP/A356 syntactic foam showed typical mechanical behaviour of metallic foams. An almost constant plateau stress (average 30.8 MPa) along with a high densification strain (around 60%) makes this foam an excellent energy absorber. Also, the foams showed a high energy absorption efficiency with a mean value of 88%. A slight increase in the syntactic foam density significantly improves its mechanical properties. As an explanation, a change in the macroscopic deformation mode was identified. The foams with a lower density deformed predominantly within a large shear band causing a decrease of compressive stress. In contrast, samples with higher density compressed in a uniform layer by layer densification. Comparison with material properties of related materials indicates that due to its poor mechanical strength the expanded perlite does not directly enhance the mechanical properties of the syntactic foam. However, it plays an important role as a low cost space holder with good wettability which can remain in structure because of its very low density and inertness.

#### Acknowledgements

We acknowledge the assistance of staff in the electron microscope and X-ray units at the University of Newcastle, NSW, Australia.

#### References

- [1] G.H. Wu, Z.Y. Dou, D.L. Sun, L.T. Jiang, B.S. Ding, B.F. He, *Scr. Mater.* 56 (2007) 221–224.
- [2] X.F. Tao, Y.Y. Zhao, *Scr. Mater.* 61 (2009) 461–464.
- [3] Z.Y. Dou, L.T. Jiang, G.H. Wu, Q. Zhang, Z.Y. Xiu, G.Q. Chen, *Scr. Mater.* 57 (2007) 945–948.

- [4] L.P. Zhang, Y.Y. Zhao, *J. Compos. Mater.* 41 (2007) 2105–2117.
- [5] A. Daoud, *Mater. Sci. Eng. A* 525 (2009) 7–17.
- [6] L. Peroni, M. Scapin, M. Avalue, J. Weise, D. Lehmhus, *Mater. Sci. Eng. A* 552 (2012) 364–375.
- [7] I.N. Orbulov, J. Dobranszky, A. Nemeth, *J. Mater. Sci.* 44 (2009) 4013–4019.
- [8] D.D. Luong, O.M. Strbiklil, V.H. Hammond, N. Gupta, K. Cho, *J. Alloys Compd.* 550 (2013) 412–422.
- [9] G. Castro, S.R. Nutt, X. Wenchen, *Mater. Sci. Eng. A* 578 (2013) 222–229.
- [10] X.F. Tao, L.P. Zhang, Y.Y. Zhao, *Mater. Des.* 30 (2009) 2732–2736.
- [11] I.N. Orbulov, J. Ginsztler, *Acta Polytech. Hung.* 9 (2012) 43–56.
- [12] T. Fiedler, H.S. Richards, I.V. Belova, A. Öchsner, G.E. Murch, *Exp. Therm. Fluid Sci.* 44 (2013) 637–641.
- [13] T. Fiedler, E. Solórzano, A. Öchsner, *Mater. Lett.* 62 (2008) 1204–1207.
- [14] A.H. Brothers, D.C. Dunand, Q. Zheng, J. Xu, *J. Appl. Phys.* 102 (2007) 0235081–0235086.
- [15] C.T.E. Brunetona, N. Gras-Naulinb, A. Cosculluela, *Carbon* 40 (2002) 1919–1927.
- [16] I.N. Orbulov, *Mater. Sci. Eng. A* 583 (2013) 11–19.
- [17] P.K. Rohatgi, J.K. Kim, N. Gupta, S. Alaraj, A. Daoud, *Compos. Part A: Appl. Sci. Manuf.* 37 (2006) 430–437.
- [18] A. Daoud, M.T. Abou El-khair, M. Abdel-Aziz, P. Rohatgi, *Compos. Sci. Technol.* 67 (2007) 1842–1853.
- [19] D.P. Mondal, S. Das, N. Ramakrishnan, K. Uday Bhasker, *Compos. Part A: Appl. Sci. Manuf.* 40 (2009) 279–288.
- [20] X.F. Tao, Y.Y. Zhao, *Mater. Sci. Eng. A* 549 (2012) 228–232.
- [21] D.K. Balch, D.C. Dunand, *Acta Mater.* 54 (2006) 1501–1511.
- [22] R.A. Palmer, K. Gao, T.M. Doan, L. Green, G. Cavallaro, *Mater. Sci. Eng. A* 464 (2007) 85–92.
- [23] C. Gaillard, J.F. Despois, A. Mortensen, *Mater. Sci. Eng. A* 374 (2004) 250–262.
- [24] J.K. Cochran, *Curr. Opin. Solid State Mater. Sci.* 3 (1998) 474–479.
- [25] M. Roulia, K. Chassapis, C. Fotinopoulos, T. Savvidis, D. Katakis, *Spill Sci. Technol. Bull.* 8 (2003) 425–431.
- [26] İ.B. Topçu, B. İşıkdag, *J. Mater. Process. Technol.* 204 (2008) 34–38.
- [27] M. Singh, M. Garg, *Constr. Build. Mater.* 5 (1991) 75–81.
- [28] E. De Langer, F. Wyss, I.N. Orbulov, *Period. Polytech. Mech. Eng.* 55 (2011) 29–37.
- [29] M. Jamei, H. Guiras, Y. Chtourou, A. Kallel, E. Romero, I. Georgopoulos, *Eng. Geol.* 122 (2011) 261–271.
- [30] Q.G. Wang, *Metall. Mater. Trans. A* 34 (2003) 2887–2899.
- [31] J.B. Ferguson, J.A. Santa Maria, B.F. Schultz, P.K. Rohatgi, *Mater. Sci. Eng. A* 582 (2013) 423–432.
- [32] D. Kramar, V. Bindiganavile, *Cem. Concr. Compos.* 37 (2013) 205–214.
- [33] P.K. Rohatgi, R.Q. Guo, H. Iksan, E.J. Borchelt, R. Asthana, *Mater. Sci. Eng. A* 244 (1998) 22–30.
- [34] D.K. Balch, J.G. O'Dwyer, G.R. Davis, C.M. Cady, G.T. Gray III, D.C. Dunand, *Mater. Sci. Eng. A* 391 (2005) 408–417.
- [35] W. Liu, U. Köster, *J. Mater. Sci. Lett.* 15 (1996) 2188–2191.
- [36] W. Liu, U. Köster, *Mater. Sci. Eng. A* 210 (1996) 1–7.
- [37] N. Yoshikawa, Y. Watanabe, Z.M. Vellozo, A. Kikuchi, S. Taniguchi, *J. Jpn. Inst. Met.* 63 (1999) 312–318.
- [38] M.C. Breslin, J. Ringnalda, L. Xu, M. Fuller, J. Seeger, G.S. Daehn, T. Otani, H.L. Fraser, *Mater. Sci. Eng. A* 195 (1995) 113–119.
- [39] N. Yoshikawa, A. Hattori, S. Taniguchi, *Mater. Sci. Eng. A* 342 (2003) 51–57.
- [40] N. Yoshikawa, A. Hattori, S. Taniguchi, *Mater. Trans.* 46 (2005) 842–845.
- [41] K. Michelsen, H. De Raedt, J.T.M. De Hosson, *Adv. Imag. Elect. Phys.* 125 (2003) 119–194.
- [42] Q. Zhang, P.D. Lee, R. Singh, G. Wu, T.C. Lindley, *Acta Mater.* 57 (2009) 3003–3011.
- [43] X. Tao, L. Zhang, Y. Zhao, *Materials Science and Technology (MS&T)*, Pittsburgh, PA, 2008, pp. 2587–2594.
- [44] M. Kiser, M.Y. He, F.W. Zok, *Acta Mater.* 47 (1999) 2685–2694.
- [45] Q. Fabrizio, A. Boschetto, L. Rovatti, L. Santo, *Mater. Lett.* 65 (2011) 2558–2561.
- [46] D.P. Mondal, M.D. Goel, S. Das, *Mater. Des.* 30 (2009) 1268–1274.
- [47] M.F. Ashby, A. Evans, N.A. Fleck, L.J. Gibson, J.W. Hutchinson, H.N.G. Wadley, *Mater. Des.* 23 (2002) 119.
- [48] ISO, 13314, Switzerland, 2011.
- [49] C. San Marchi, J.F. Despois, A. Mortensen, *Acta Mater.* 52 (2004) 2895–2902.
- [50] K.Y.G. McCullough, N.A. Fleck, M.F. Ashby, *Acta Mater.* 47 (1999) 2323–2330.
- [51] L. Peroni, M. Scapin, M. Avalue, J. Weise, D. Lehmhus, J. Baumeister, M. Busse, *Adv. Eng. Mater.* 14 (2012) 909–918.
- [52] M. Alizadeh, M. Mirzaei-Aliabadi, *Mater. Des.* 35 (2012) 419–424.
- [53] M.D. Goel, M. Peroni, G. Solomos, D.P. Mondal, V.A. Matsagar, A.K. Gupta, M. Larcher, S. Marburg, *Mater. Des.* 42 (2012) 418–423.
- [54] D.-w. Huo, J. Yang, X.-y. Zhou, H. Wang, T.-k. Zhang, *Trans. Nonferrous Met. Soc. China* 22 (2012) 85–89.
- [55] H. Bafti, A. Habibolahzadeh, *Mater. Des.* 52 (2013) 404–411.
- [56] N. Michailidis, F. Stergioudi, A. Tsouknidas, E. Pavlidou, *Mater. Sci. Eng. A* A528 (2011) 1662–1667.
- [57] N. Michailidis, F. Stergioudi, A. Tsouknidas, *Mater. Sci. Eng. A* 528 (2011) 7222–7227.
- [58] A.F. Bastawros, H. Bart-Smith, A.G. Evans, *J. Mech. Phys. Solids* 48 (2000) 301–322.
- [59] J. Kadkhodapour, S. Raeisi, *Comput. Mater. Sci.* 83 (2014) 137–148.